

1 Revision 2

2 **Magnetism and equation of states of fcc FeH_x at high pressure**

3 Word Count: 6793

4 Hitoshi Gomi^{a,b,*}, Kei Hirose^{a,b}

5 ^a Earth-Life Science Institute, Tokyo Institute of Technology, 2-12-1 Ookayama,
6 Meguro, Tokyo, 152-8550, Japan

7 ^b Department of Earth and Planetary Science, The University of Tokyo, 7-3-1 Hongo,
8 Bunkyo, Tokyo, 113-0033, Japan

9 * Corresponding author. *E-mail address*: hitoshi.gomi@eps.s.u-tokyo.ac.jp

10

11 **ABSTRACT**

12 Hydrogen is a strong candidate for light alloying elements in the terrestrial cores.
13 Previous first-principles studies on non-stoichiometric hexagonal close-packed (hcp)
14 and double hexagonal close-packed (dhcp) FeH_x predicted a discontinuous volume
15 expansion across the magnetic phase transition from non-magnetic (NM) or
16 antiferromagnetic (AFM) to ferromagnetic (FM) state with increasing the hydrogen
17 content, x at 0 K. However, previous high pressure and temperature neutron diffraction
18 experiments on face-centered cubic (fcc) FeH_x did not show such nonlinearity. The
19 discrepancy between theory and experiment may be due to differences in the crystal
20 structure, magnetism, or temperature. In this study, we computed the equation of states
21 for fcc FeH_x by using the Korringa-Kohn-Rostoker method combined with the
22 coherent potential approximation (KKR-CPA). In addition to the four types of
23 ground-state magnetism (FM, AFM-I, AFM-II, and NM), we also calculated the local
24 magnetic disorder (LMD) state, which approximates the paramagnetic (PM) state with
25 local spin moment above the Curie temperature. The results show that even though FM,
26 AFM-I, AFM-II, and NM calculations predict a discontinuity in the volume at 0 K, the
27 volume becomes continuous above the Curie temperature, consistent with the previous
28 high-temperature experiment. From the enthalpy comparison at 0 K, FM fcc FeH ($x =$
29 1) undergoes the NM state above ~ 48 GPa. The magnetic transition pressure decreases
30 with decreasing hydrogen content. Therefore, below the magnetic transition pressure,
31 local spin moments affect the density and elastic wave velocity of fcc FeH_x , which may
32 be important for small terrestrial bodies such as Mercury and Ganymede. On the other
33 hand, at the Earth's core pressure above 135 GPa, fcc FeH_x becomes NM. Thus, we
34 calculated the density and bulk sound velocity as a function of pressure at 0 K for NM

35 fcc FeH_x. The density at 360 GPa decreases with increasing hydrogen content, with
36 FeH_{0.5} best matching the preliminary reference Earth model (PREM) of the inner core.
37 Since the density decreases with increasing temperature, this value constrains the upper
38 limit of hydrogen content, assuming the inner core is fcc FeH_x. On the other hand, the
39 bulk sound velocity at 360 GPa increases with increasing hydrogen content, with
40 FeH_{0.3} best matching the PREM, which may give a lower bound. Assuming that the
41 Poisson's ratio of the FeH_x alloy is equal to that of the inner core, we examined the
42 effects of temperature on density and bulk sound velocity. The results suggest that the
43 fcc FeH_x alloy alone cannot explain the inner core density and bulk sound velocity
44 simultaneously unless the temperature is extremely low ($T < 4000$ K).

45 **Keywords:** FeH_x, magnetism, equation of states, KKR-CPA, inner core

46 INTRODUCTION

47 The Earth's core is thought to contain a certain amount of light elements in addition
48 to iron and nickel (e.g., Hirose et al. 2021). Recent studies of metal-silicate partitioning
49 have indicated that the Earth's core may contain hydrogen (Tagawa et al. 2021; Yuan
50 and Steinle-Neumann 2020; Li et al. 2020). Hydrogen alloying is also essential to the
51 cores of terrestrial planets other than Earth. For example, Mercury and Ganymede have
52 dipole magnetic fields. If these fields are generated by the convective motion of the
53 liquid core, the melting temperature of the core must be lower than pure iron. Among
54 the light-element candidates for the core, sulfur (e.g., Mori et al. 2017) and hydrogen
55 (e.g., Sakamaki et al. 2009) significantly decrease the melting temperature. Therefore,
56 Ganymede's core may contain these light elements (Shibazaki et al. 2011).

57 Experiments on iron-hydrogen systems are technically more complicated than those

58 on other iron alloys. For example, when the FeH_x alloy synthesized under high
59 pressure is depressurized, the hydrogen degasses, and chemical analysis of the
60 recovered sample cannot be performed. Therefore, the following equation (1) is often
61 used to estimate the hydrogen concentration from the volume of the iron alloy obtained
62 from in-situ X-ray observation using the assumption that the volume of FeH_x is
63 proportional to the hydrogen concentration (e.g., Fukai 2006).

$$64 \quad x = \frac{V_{\text{FeH}_x} - V_{\text{Fe}}}{\Delta V_H} \quad (1)$$

65 where V_{FeH_x} is the measured volume of FeH_x , V_{Fe} is the volume of iron at the same
66 temperature and pressure conditions as the reference, and ΔV_H is the volume expansion
67 due to hydrogen alloying. This equation has been validated for several metal-hydrogen
68 alloys with face-centered cubic (fcc) structure (Fukai 2006). However, it may not be
69 possible to interpolate a straight line between the Fe and FeH end members if they
70 have different crystal and/or magnetic structures.

71 Pure iron ($x = 0$) has three different polymorphs: body-centered cubic (bcc), fcc, and
72 hexagonal close-packed (hcp) structure. At the ambient conditions, the bcc structure is
73 stable. Bcc Fe is ferromagnetic (FM) with the Curie temperature of $T_C = 1043$ K, and
74 its pressure dependence is negligible (Leger et al. 1972). When compressed at room
75 temperature, it undergoes a phase transition to the hcp phase at ~ 15 GPa. The
76 magnetism of hcp Fe is considered to be nonmagnetic (NM) or antiferromagnetic
77 (AFM) (Nasu et al. 2002; Steinle-Neumann et al. 2004). The hcp structure is stable at
78 the Earth's inner core pressure (P) and temperature (T) conditions (e.g., Tateno et al.
79 2010). On the other hand, at pressures below 90 GPa, the fcc structure becomes stable
80 at high temperatures (Komabayashi and Fei 2010). The fcc stability region includes the
81 P - T conditions of the core of planets and satellites such as the Moon, Ganymede,

82 Mercury, and Mars (see e.g., Tsujino et al. 2013). Metastable fcc Fe at ambient
83 condition is considered to be in first-kind antiferromagnetic (AFM-I) or
84 spin-density-wave (SDW) state (Abraham et al. 1962; Tsunoda 1989).

85 The crystal structure and magnetism of stoichiometric FeH ($x = 1$ for FeH_x) have
86 been studied by theoretical calculations and high-pressure experiments on iron
87 saturated with hydrogen. At the ambient conditions, bcc Fe does not react with
88 hydrogen, but the solubility of hydrogen increases due to the effects of temperature,
89 pressure, and structural phase transition (Sugimoto and Fukai 1992). Therefore, the
90 stability field of bcc Fe is smaller in a hydrogen-saturated system than in a
91 hydrogen-free system. At room temperature, double hexagonal close-packed (dhcp)
92 FeH becomes stable above 3.5 GPa (e.g., Badding et al. 1991). This dhcp FeH is FM
93 (e.g., Schneider et al. 1991; Mitsui et al. 2010). The Curie temperature of dhcp FeH is
94 expected to be $T_C \sim 1200$ K at ambient pressure and decrease rapidly with increasing
95 pressure (Gomi et al. 2018). Upon pressurization, FM dhcp FeH undergoes a magnetic
96 transition to NM (Gomi et al. 2018). Like fcc Fe, fcc FeH has a stable region at high
97 temperatures. Furthermore, fcc FeH can be obtained by compressing dhcp FeH at room
98 temperature (Isaev et al. 2007; Thompson et al. 2018; Kato et al., 2020). The
99 Mössbauer spectroscopy of fcc FeH at 47 GPa and 300 K suggests it is either NM or
100 AFM (Narygina et al. 2011). On the other hand, the experimentally determined
101 equation of state of fcc FeH is consistent with first-principles calculations with FM at
102 pressures below ~ 60 GPa (Kato et al. 2020). Thus, the ground state magnetism of
103 metastable fcc FeH near ambient pressure is FM, as for dhcp FeH, and may undergo a
104 magnetic transition to NM upon compression.

105 As stated above, Fe and FeH have different crystal structures and magnetic states

106 even at the same P - T conditions. Therefore, structural and/or magnetic transitions
107 should occur when the hydrogen concentration (x) is changed. Gomi et al. (2018)
108 compared the relative stability of FM/NM hcp/dhcp FeH_x from first-principles
109 calculations. Similarly, León et al. (2020) compared the relative stability of FM/AFM
110 hcp FeH_x . Both studies showed that NM or AFM states are stable at low hydrogen
111 concentrations, and phase transitions to FM occur as the hydrogen concentration
112 increases. Importantly, a significant volume discontinuity accompanies this magnetic
113 transition since NM and AFM phases have a smaller volume than the FM phase. Such
114 a large volume change implies a breakdown of Eq. (1) for hcp and dhcp FeH_x at 0 K.
115 However, high P - T neutron diffraction experiments on fcc FeH_x by Ikuta et al. (2019)
116 confirmed a linear relationship between hydrogen concentration and volume expansion
117 (Eq. 1). In this study, we calculated the equation of state for fcc FeH_x using the
118 Korringa-Kohn-Rostoker method combined with the coherent potential approximation
119 (KKR-CPA). FM, NM, AFM-I, and AFM-II were considered as the ground state
120 magnetism. We further calculated the local magnetic disorder (LMD) state to examine
121 the effect of temperature on magnetism. We also calculated NM hcp and dhcp FeH_x to
122 investigate the effect of different crystal structures on the equation of state.

123 **METHODS**

124 We performed first-principles calculations for FeH_x similarly to Gomi et al. (2018).
125 The Kohn-Sham equation was solved by the Korringa-Kohn-Rostoker (KKR) method
126 (Akai 1989). A Perdew-Burke-Ernzerhof (PBE)-type generalized gradient
127 approximation (GGA) was used for the exchange-correlation potential (Perdew et al.
128 1996). Relativistic effects were taken into account in the scalar relativistic

129 approximations. The wavefunction was computed up to $l = 2$, where l is the angular
130 momentum quantum number. The coherent potential approximation (CPA) was used to
131 represent hydrogen atoms randomly occupying octahedral interstitial sites. The
132 hydrogen concentration x was changed from 0 (Fe) to 1 (FeH) in increments of 0.1. For
133 fcc FeH_x, spin-polarized and non-spin-polarized calculations were performed. Five
134 types of spin configurations were calculated: FM, NM, AFM-I, AFM-II, and LMD
135 states, in which the up and down spins form a random alloy, simulating a state with a
136 local spin moment above the characteristic magnetic transition temperature (i.e., Curie
137 or Néel temperature) (e.g., Akai and Dederichs 1993; Gomi et al. 2018). To calculate
138 the AFM states, we considered two different spin configurations shown in Figure (S1),
139 which are drawn by VESTA (Momma and Izumi 2011). The calculation cell for AFM-I
140 with the same spins in the (001) plane is the bottom-centered orthorhombic lattice and
141 contains 2FeH_x. The k -points of this calculation are sampled 1050 points in the
142 irreducible Brillouin zone. The calculation cell for the AFM-II with the same spin in
143 the (111) plane is a rhombohedral lattice and contains 2FeH_x. The other three
144 configurations (FM, NM, and LMD) are also calculated with this rhombohedral
145 calculation cell. The k -points were sampled at 1313 points in the irreducible Brillouin
146 zone. The muffin-tin approximation was used. To maximize the muffin-tin radius (r) of
147 Fe site, we adopted $r_{\text{Fe}} = \sqrt{2}a_{\text{fcc}}/4$ for the Fe, and $r_{\text{H}} = (2 - \sqrt{2})a_{\text{fcc}}/4$ for the H,
148 where a_{fcc} is the lattice parameter of the fcc lattice of the same volume. In this case, the
149 total volume of the muffin-tin spheres is 79.3% of the calculated cell. Furthermore, we
150 also performed NM calculations for hcp and dhcp FeH_x. In each volume, we optimized
151 the axial ratio c/a from the total energy. We set the muffin-tin radius smaller than the
152 fcc FeH_x calculations, with keeping $r_{\text{H}}/r_{\text{Fe}} = \sqrt{2} - 1$. As a result, the total volume of

153 the muffin-tin spheres becomes 73.2% of the calculation cell. For calculating hcp and
154 dhcp, we performed a k -point sampling of 640 and 280 points, respectively, in the
155 irreducible Brillouin zone. The size of the calculation cell ranged from 50 to 120 Bohr³
156 per chemical formula with 2 Bohr³ steps. The total energy was fitted to the Vinet
157 equation of state.

$$158 \quad E(V) = \frac{2K_0V_0}{(K'_0-1)^2} \left\{ 2 - \left[5 + 3 \left(\frac{V}{V_0} \right)^{\frac{1}{3}} (K'_0 - 1) - 3K'_0 \right] \exp \left[-\frac{3}{2} (K'_0 - 1) \left[\left(\frac{V}{V_0} \right)^{\frac{1}{3}} - 1 \right] \right] \right\} + E_0 \quad (2)$$

159 where E is the total energy, V is the volume, K and K' are the isothermal bulk modulus
160 and its pressure derivative. Subscript 0 indicates the zero-pressure value. All data were
161 fitted for NM calculations. Data with non-zero local spin moments was used for
162 spin-polarized calculations (FM, LMD, AFM-I, and AFM-II). The pressure and
163 isothermal bulk modulus can be calculated from the obtained fitting parameters.

$$164 \quad P(V) = 3K_0 \left(\frac{V_0}{V} \right)^{\frac{2}{3}} \left[1 - \left(\frac{V}{V_0} \right)^{\frac{1}{3}} \right] \exp \left\{ \frac{3}{2} (K'_0 - 1) \left[1 - \left(\frac{V}{V_0} \right)^{\frac{1}{3}} \right] \right\} \quad (3)$$

$$165 \quad K_T(V) = K_0 \left(\frac{V_0}{V} \right)^{\frac{2}{3}} \left[1 + \left\{ \frac{3}{2} (K'_0 - 1) \left(\frac{V}{V_0} \right)^{\frac{1}{3}} + 1 \right\} \left[1 - \left(\frac{V}{V_0} \right)^{\frac{1}{3}} \right] \right] \exp \left[\frac{3}{2} (K'_0 - 1) \left\{ 1 - \left(\frac{V}{V_0} \right)^{\frac{1}{3}} \right\} \right] \quad (4)$$

166 Note that adiabatic bulk modulus can be described as $K_S = (1 + \alpha\gamma T)$, where α is the
167 thermal expansion coefficient and γ is the Grüneisen parameter. At 0 K, K_S is equal to
168 K_T . And it is reasonable to approximate $K_S \sim K_T$ at 300 K, whereas the difference
169 between K_T and K_S becomes significant at high temperature relevant to terrestrial
170 cores.

171 We can roughly estimate the Curie temperature by comparing the relative enthalpy
172 between FM and LMD states (Sato et al. 2003).

$$173 \quad T_c(P) = \frac{2}{3k_B} (\Delta E(P) + P\Delta V) \quad (5)$$

174 where T_c is the Curie temperature, P is pressure, k_B is the Boltzmann's constant, ΔE

175 and ΔV are energy and volume difference between FM and LMD states, respectively.

176 **RESULTS**

177 Figure S2-12 shows the results for fcc FeH_x. Note that the local spin moment of FM
178 is almost equal to the bulk spin moment, while the bulk spin moments of AFM-I,
179 AFM-II, and LMD are zero. The local spin moment decreases with compression. The
180 disappearance of the spin moment occurs at the point where the total energy curves of
181 the magnetic phases (FM, AFM-I, AFM-II, and LMD) intersect the total energy curve
182 of NM. At this point, the local magnetic moment of FM abruptly drops to zero, while
183 that of AFM-I, AFM-II, and LMD decrease slowly. The magnitude of the spin moment
184 in the same volume decreases with increasing hydrogen concentration, which is
185 consistent with León et al. (2020).

186 Figure S2-12 (b) shows the total energy of fcc FeH_x. Figure S13 shows the results of
187 NM hcp and dhcp FeH_x calculated in the same volume range as fcc FeH_x. The symbols
188 are the calculation results, and the solid lines are the fitting curves. Obtained fitting
189 parameters are summarized in Table S1 and S2. The E_0 of fcc FeH is in the order of
190 FM, AFM-II, LMD, AFM-I, NM from the lowest. Note that AFM-II is more stable
191 than AFM-I, consistent with previous first-principles results by Kato et al. (2020). On
192 the other hand, the total energy of Fe is in the order of FM, LMD, AFM-I, AFM-II,
193 NM from the lowest energy; AFM-I is more stable than AFM-II. Figure 1 shows the
194 pressure-volume relationship obtained in this study compared with previous
195 experiments (Narygina et al. 2011; Tagawa et al. 2022; Kato et al. 2020; Dewaele et al.
196 2006; Fei et al. 2016). The NM fcc FeH results are consistent with previous
197 experiments at high pressure, while they are inconsistent at low pressure. The

198 experimental results at low pressure are consistent with the calculated results of FM
199 fcc FeH.

200 The relative stability of each phase can be discussed from the comparison of
201 enthalpies, which are plotted in Figure S2-12 (c) and (d). First, we discuss fcc Fe
202 endmember. The enthalpy of fcc Fe (Fig. S2c) shows that FM is the most stable at 0
203 GPa and AFM-I is the next most stable. However, the experimentally obtained ground
204 state magnetism of metastable fcc Fe is not FM. Abraham et al. (1962) performed
205 neutron diffraction experiments on fcc Fe precipitated in Cu and reported its magnetic
206 structure as AFM-I. Later, Tsunoda (1989) reported that the ground state magnetism of
207 precipitated fcc Fe is not AFM-I, but a more complicated SDW state. According to the
208 previous first-principles calculations, fcc Fe has FM, NM, AFM, and SDW energies in
209 the range of a few mRy and is also sensitive to the lattice parameters (Tsetseris 2005).
210 The present results also show that the enthalpy difference between FM and AFM-I is
211 only ~2 mRy, and including NM and AFM-II, it is within 4 mRy. From the enthalpy
212 difference between FM and LMD, the Curie temperature can be roughly estimated (Fig.
213 S2-12d). The Curie temperature of FM fcc Fe was estimated to be $T_C = 189$ K (Fig.
214 S2d), which is close to the experimental Néel temperature of SDW fcc Fe of $T_N = 67$ K
215 (Onodera et al. 1994) (Fig. 2). Due to the above difficulties and the fact that the present
216 work does not involve the SDW calculations, it may not be possible to correctly
217 estimate the magnetism of the ground state of fcc FeH_x with low hydrogen
218 concentration by comparing the enthalpies. However, due to the low Curie and Néel
219 temperatures, metastable fcc FeH_x is expected to be a paramagnetic (PM) state with a
220 local spin moment at room temperature and zero pressure. Then, we discuss fcc FeH
221 endmember. For fcc FeH, FM stability increase compared with fcc Fe, which suggests

222 that SDW may not appear at high hydrogen concentration and FM becomes stable.
223 From comparing the enthalpies of FM and NM, the FM-NM transition is expected at P
224 ~ 48 GPa (Fig. S12c). The enthalpy difference between FM and LMD corresponds to
225 the Curie temperature of $T_C = 1088$ K at 0 GPa. This value is comparable to the Curie
226 temperature of $T_C = 1043$ K for bcc Fe, suggesting the FM stability against the
227 temperature. However, it decreases with pressure (Fig. S12d), which is consistent with
228 the previous Mössbauer measurement at 47 GPa and 300 K that indicates NM or AFM
229 state (Narygina et al. 2011). Finally, we discuss the effects of hydrogen concentration,
230 pressure, and temperature on the stability of FM fcc FeH_x . As for the FM-NM
231 transition, its pressure decreases from $P \sim 48$ GPa (FeH) with decreasing hydrogen
232 content. Similarly, the Curie temperature decreases with decreasing hydrogen
233 concentration and increasing pressure (Fig. 2). Decreasing FM stability with increasing
234 temperature, increasing pressure, or decreasing hydrogen concentration follows the
235 same trend as in our previous study of hcp FeH_x and dhcp FeH_x (Gomi et al. 2018).

236 **DISCUSSION**

237 In hcp FeH_x and dhcp FeH_x , a discontinuous volume change with the NM (or
238 AFM)-FM magnetic transition is predicted from first-principles calculations when the
239 hydrogen concentration is varied (Gomi et al. 2018; León et al. 2020). However, in the
240 high P - T neutron diffraction experiment on fcc FeH_x by Ikuta et al. (2019), the volume
241 increases linearly with increasing hydrogen concentration, and no discontinuity is
242 observed. There are two possible reasons for this discrepancy between theory and
243 experiment. The first is that fcc Fe has SDW (or AFM-I like) magnetism at 0 K. The
244 second is that previous calculations (Gomi et al. 2018; León et al. 2020) are done at 0

245 K, while Ikuta et al. (2019) is a high-temperature experiment at 750-1200 K. Figure 3
246 shows our calculated volumes of FM, NM, and LMD fcc FeH_x compared with previous
247 experiments (Machida et al. 2014; Ikuta et al. 2019; Shito et al. in press). Ikuta et al.
248 (2019) plotted the measured volume of fcc FeH_x minus the calculated volume of fcc Fe
249 at the same *P-T* conditions (Tsujino et al. 2013) to see the effect of volume expansion
250 due to hydrogen only. To make a fair comparison, we also calculated the volume of fcc
251 FeH_x at 3.8-12.3 GPa and plotted the volume difference between present fcc FeH_x and
252 fcc Fe calculated from the previous experimental equation of state (Tsujino et al. 2013).
253 In this way, the effect of magnetism and hydrogen on the volume can be discussed.
254 First, the NM results do not reproduce the Ikuta et al. (2019)'s experiments at all
255 hydrogen concentrations. Second, FM reproduces Ikuta et al. (2019) in the region of x
256 ≥ 0.7 but overestimates at $x \leq 0.2$. In contrast, the LMD reproduces the volume of Ikuta
257 et al. (2019) over a wide range of hydrogen concentrations. LMD simulates a PM state
258 with the local spin moment at temperatures higher than the Curie or Néel temperature
259 of FM, AFM and, SDW states. In the region of low hydrogen concentration ($x \leq 0.2$),
260 the volumes of LMD fcc FeH_x show good agreements with previous experiments
261 (Ikuta et al. 2019) because the Curie temperature (Fig. 2) is lower than the temperature
262 range of the experiments. Similarly, for $x \geq 0.7$, the Curie temperature and
263 experimental temperature conditions are close, so the calculated results of LMD or FM
264 are close to the results of Ikuta et al. (2019). Thus, no discontinuous volume change is
265 observed when the temperature is higher than the Curie (or Néel) temperature, even
266 though magnetism considerably influences the volume below the FM-NM transition
267 pressure $P \sim 48$ GPa for fcc FeH.

268 Let us discuss the difference in volume depending on the crystal structures. We

269 found that fcc FeH becomes NM at $P > \sim 48$ GPa. Also, dhcp FeH is NM at $P > \sim 65$
270 GPa (Gomi et al. 2018). For FeH_x, the stable region of NM expands as the hydrogen
271 concentration decreases, so we only need to consider NM to discuss the Earth's core,
272 whose pressure is $P \geq 135$ GPa. Figure 4 shows the volumes of NM fcc, hcp, and dhcp
273 FeH_x at 135 GPa and 360 GPa. The difference between the three crystal structures (fcc,
274 hcp, and dhcp) has little effect on the volume (Fig. 4, Table S1-4). The present results
275 are consistent with previous studies of hcp FeH_x (Caracas 2015). The dashed line in
276 Figure 3 is a linear interpolation between the experimental equation of state for hcp Fe
277 (Dewaele et al. 2006) and fcc FeH (Tagawa et al. 2022). Our results agree
278 quantitatively well with the experimental interpolation and thus support the validity of
279 Eq. 1 at the pressure at which NM becomes stable.

280 **IMPLICATIONS**

281 In order to constrain the chemical composition of the inner core, the physical
282 properties from seismic observations are compared to those obtained from experiments
283 or calculations. For example, Caracas (2015) obtained the density (ρ), longitudinal
284 velocity (V_p), and transverse velocity (V_s) for hcp FeH_x from static first-principles
285 calculations. Based on his results, Caracas (2015) argued that V_s is too high to explain
286 the preliminary reference Earth model (PREM) (Dziewonski and Anderson 1981) for
287 any value of x in hcp FeH_x. On the contrary, He et al. (2022) suggested that the
288 interstitial H atoms become a super-ionic state at high temperatures based on their ab
289 initio molecular dynamics (AIMD) simulations on hcp FeH_{0.25}, which result in a
290 significant reduction of V_s . Also, earlier experimental studies (Mao et al. 2004;
291 Shibazaki et al. 2012; Thompson et al. 2018) argued that hydrogen is a good candidate

292 for the light elements based on experimentally based extrapolation models. Mao et al.
293 (2004) and Thompson et al. (2018) measured the Debye sound velocity (V_D) by nuclear
294 resonant inelastic X-ray scattering (NRIXS). The Debye sound velocity can be
295 represented as $3/V_D^3 = 1/V_P^3 + 2/V_S^3$. V_P and V_S can be calculated by associating V_D
296 with the bulk sound velocity $V_\Phi = \sqrt{K_S/\rho} = \sqrt{V_P^2 - (4/3)V_S^2}$. Also, Shibazaki et al.
297 (2012) measured V_P of dhcp FeH by using the inelastic X-ray scattering (IXS). They
298 also estimated V_S via V_Φ . Considering that $K_S \sim K_T$ at 300 K, V_Φ (or isothermal bulk
299 modulus, K_T) can be obtained from the equation of state (Eq. 4). However, since $K_T(V)$
300 is a derivative of pressure, the extrapolation of $K_T(V)$ may have a more significant error
301 than the extrapolation of $P(V)$.

302 In this study, we calculated the density and bulk sound velocity as function of
303 pressure at 0 K using the equation of state obtained by first-principles calculations and
304 compared them with the PREM of the inner core (Dziewonski and Anderson 1981).
305 The density and bulk sound velocities of NM and LMD fcc FeH_x obtained in this study
306 are plotted as a function of pressure (Fig. 5). There is a discontinuity in the bulk sound
307 velocity between NM and LMD, which is consistent with recent V_P measurement on
308 fcc FeH (Wakamatsu et al. 2022). Therefore, if such magnetic transitions exist in
309 Ganymede and Mercury core, anomalies in elastic wave velocities may be expected.
310 Comparing the present density with the PREM at the inner core, NM fcc $\text{FeH}_{0.5}$ agreed
311 best. However, the equation of state in this study was obtained from static
312 first-principles calculations. The density expected to decrease with increasing
313 temperature. Therefore, if we assume that the Earth's inner core is composed of fcc
314 FeH_x , the results of the density place a constraint of $x < 0.5$. Similarly, NM $\text{FeH}_{0.3}$ best
315 agreed with the bulk sound velocity of PREM. Assuming that the bulk sound velocity

316 decrease with increasing temperature, the hydrogen content is restricted to $x > 0.3$.
317 Figure 6 represents the density-bulk sound velocity relationship at 360 GPa. Present
318 values for fcc Fe at 0 K show excellent agreement with hcp Fe calculated from the
319 experimental equation of state at 300 K (Dewaele et al. 2006). As the hydrogen
320 concentration increased, the density decreased, and the bulk sound velocity increased,
321 which is consistent with Caracas (2015). Previous AIMD studies (Martorell et al. 2015;
322 He et al. 2022) reported these values at 0 K, which also followed this trend, even
323 though they systematically overestimated the bulk sound velocity.

324 For the sole purpose of comparison with PREM, we also calculated density and bulk
325 sound velocity of NM fcc FeH_x at high temperature and 360 GPa. Pressure can be
326 obtained from the derivation of the Helmholtz energy (F) as follows,

$$327 \quad P(V, T) = - \left(\frac{\partial F(V, T)}{\partial V} \right)_T. \quad (6)$$

328 Therefore, once $F(V, T)$ is obtained as a function of volume and temperature, the
329 volume can be determined under arbitrary pressure and temperature conditions. The
330 Helmholtz energy can be expressed by the internal energy (U) and entropy (S).

$$331 \quad F(V, T) = U(V, T) - TS(V, T) \quad (7)$$

332 We now consider the electron and phonon contributions to U , S , and specific heat at
333 constant volume (C_V), respectively.

$$334 \quad U(V, T) = U_{ele}(V, T) + U_{vib}(V, T) \quad (8)$$

$$335 \quad S(V, T) = S_{ele}(V, T) + S_{vib}(V, T) \quad (9)$$

$$336 \quad C_V(V, T) = C_{V,ele}(V, T) + C_{V,vib}(V, T) \quad (10)$$

337 The thermodynamic parameters of the electron system can be calculated numerically
338 from the density of states (DOS) (D) (e.g. Boness et al. 1986). The internal energy of
339 the electron system is given as follows,

340
$$U_{ele}(V, T) = E_{tot}(V) + \int_{-\infty}^{\infty} D(\varepsilon, V) \varepsilon f(\varepsilon, T) d\varepsilon - \int_{-\infty}^{\infty} D(\varepsilon, V) \varepsilon f(\varepsilon, 0) d\varepsilon \quad (11)$$

341 where $E_{tot}(V)$ is the total energy obtained from the static first-principles calculations,

342 $f(\varepsilon, T)$ is the Fermi-Dirac distribution function

343
$$f(\varepsilon, T) = \frac{1}{\exp\left(\frac{\varepsilon - \mu(T)}{k_B T}\right) + 1}. \quad (12)$$

344 The chemical potential (μ) is determined so that the number of electrons n_e is

345 conserved regardless of temperature,

346
$$n_e = \int_{-\infty}^{\infty} D(\varepsilon) f(\varepsilon, T) d\varepsilon = \int_{-\infty}^{\varepsilon_F} D(\varepsilon) d\varepsilon. \quad (13)$$

347 The electronic specific heat ($C_{V,ele}$) can be calculated as

348
$$C_{V,ele}(V, T) = \left(\frac{\partial U_{ele}(V, T)}{\partial T} \right)_V. \quad (14)$$

349 The electronic entropy $S_{ele}(V, T)$ is formulated as

350
$$S_{ele}(V, T) = -k_B \int_{-\infty}^{\infty} D(\varepsilon) [f(\varepsilon, T) \ln\{f(\varepsilon, T)\} + \{1 - f(\varepsilon, T)\} \ln\{1 - f(\varepsilon, T)\}] d\varepsilon. \quad (15)$$

352 The thermodynamic parameters of the phonons are calculated from the quasi-harmonic

353 approximation and the Debye model. The vibrational internal energy is calculated by

354
$$U_{vib}(V, T) = \frac{9}{8} n k_B \Theta_D(V) + 3 n k_B T D_3\left(\frac{\Theta_D(V)}{T}\right) \quad (16)$$

355 where n is the number of atoms, $\Theta_D(V)$ is the Debye temperature, $D_3(z)$ is the Debye

356 function (e.g. Moruzzi et al. 1988).

357
$$D_3(z) = \frac{3}{z^3} \int_0^z \frac{x^3}{\exp(x) - 1} dx \quad (17)$$

358 The vibrational specific heat ($C_{V,vib}$) can be expressed as

359
$$C_{V,vib}(V, T) = 9 n k_B \left(\frac{T}{\Theta_D(V)} \right)^3 \int_0^{\Theta_D(V)/T} \frac{x^4 \exp(x)}{(\exp(x) - 1)^2} dx. \quad (18)$$

360 The vibrational entropy is as follows

361
$$S_{vib}(V, T) = 3nk_B \left[\frac{4}{3} D_3 \left(\frac{\Theta_D(V)}{T} \right) - \ln \left\{ 1 - \exp \left(- \frac{\Theta_D(V)}{T} \right) \right\} \right]. \quad (19)$$

362 Therefore, we can calculate the vibrational Helmholtz energy in terms of the Debye
363 temperature $\Theta_D(V)$. Applying the quasi-harmonic approximation, the Debye
364 temperature can be obtained for isotropic materials as follows (e.g. Blanco et al. 2004)

365
$$\Theta_D(V) = \frac{\hbar}{k_B} (6\pi^2 \sqrt{V} n)^{\frac{1}{3}} g(\sigma) \sqrt{\frac{K_S(V, T)}{M}} \quad (20)$$

366 where $K_S(V, T)$ is the adiabatic bulk modulus. We assume that the Debye temperature
367 depends only on the volume. Therefore, we substituted $K_T(V, 0)$ for $K_S(V, T)$ in Eq (20).
368 Also, $g(\sigma)$ is a function of Poisson's ratio (σ) (e.g. Francisco et al. 1998).

369
$$g(\sigma) = \left\{ 3 \left[2 \left(\frac{2}{3} \frac{1+\sigma}{1-2\sigma} \right)^{\frac{3}{2}} + \left(\frac{1}{3} \frac{1+\sigma}{1-\sigma} \right)^{\frac{3}{2}} \right]^{-1} \right\}^{\frac{1}{3}} \quad (21)$$

370 Poisson's ratio can be determined from the bulk modulus and shear modulus.
371 However, the shear modulus is not calculated in this study. Instead, we assume that
372 the Poisson's ratio of fcc FeH_x is identical to that of the inner core, σ_{PREM} . Bulk sound
373 velocity is expressed by the adiabatic bulk modulus and density.

374
$$V_{\Phi}(V, T) = \sqrt{\frac{K_S(V, T)}{\rho(V)}} \quad (22)$$

375 Adiabatic bulk modulus can be obtained from isothermal bulk modulus (K_T), thermal
376 expansion coefficient (α), and Grüneisen parameter (γ) as follows,

377
$$K_S(V, T) = (1 + \alpha(V, T)\gamma(V, T)T)K_T(V, T). \quad (23)$$

378 Isothermal bulk modulus and thermal expansion coefficient are computed by using
379 numerical differentiation

380
$$K_T(V, T) = -V \left(\frac{\partial P(V, T)}{\partial V} \right)_T = V \left(\frac{\partial^2 F(V, T)}{\partial V^2} \right)_T \quad (24)$$

381
$$\alpha(V, T) = \frac{1}{V} \left(\frac{\partial V}{\partial T} \right)_P \quad (25)$$

382 Grüneisen parameter is expressed via the thermodynamic relation as follows

$$383 \quad \gamma(V, T) = \frac{\alpha(V, T) K_T(V, T)}{c_V(V, T) \rho(V)} \quad (26)$$

384 A necessary and sufficient condition for fcc FeH_x alloys to be a candidate of solo
385 constituent of the inner core is its density, bulk sound velocity, and Poisson's ratio to
386 match the PREM. In this study, we calculate the density and bulk sound velocity of fcc
387 FeH_x with the assumption that Poisson's ratio of fcc FeH_x is equal to that of PREM.
388 Therefore, it is a necessary condition that calculated density and bulk sound velocity
389 account for these values in the inner core, simultaneously, even though it is not a
390 sufficient condition. Note also that, because of the assumption of Poisson's ratio, the
391 present equation of state at high temperatures may not match the actual equation of
392 state for fcc FeH_x.

393 We plotted the density and bulk sound velocity of fcc FeH_x at $P = 360$ GPa and $T =$
394 4000, 5500, and 7000 K. As expected, density and bulk sound velocity decreases with
395 increasing temperature. However, these temperature effects are too strong to explain
396 the PREM, even at $T = 4000$ K. These results indicate that density and bulk sound
397 velocity of the Earth's inner core cannot be satisfied simultaneously by fcc FeH_x alone,
398 unless the inner core temperature is lower than 4000 K.

399 **ACKNOWLEDGMENTS AND FUNDING**

400 This work was supported by JSPS MEXT/KAKENHI Grant Number 20K22365 and
401 22K03754. We thank three anonymous reviewers for their constructive comments and
402 suggestions.

403 **REFERENCES CITED**

- 404 Abrahams, S. C., Guttman, L., and Kasper, J. S. (1962). Neutron diffraction
405 determination of antiferromagnetism in face-centered cubic (γ) iron. Physical
406 Review, 127(6), 2052.
- 407 Akai, H. (1989). Fast Korringa-Kohn-Rostoker coherent potential approximation and
408 its application to FCC Ni-Fe systems. Journal of Physics: Condensed Matter,
409 1(43), 8045.
- 410 Akai, H., and Dederichs, P. H. (1993). Local moment disorder in ferromagnetic alloys.
411 Physical Review B, 47(14), 8739.
- 412 Badding, J. V., Hemley, R. J., and Mao, H. K. (1991). High-pressure chemistry of
413 hydrogen in metals: In situ study of iron hydride. Science, 253(5018), 421-424.
- 414 Blanco, M. A., Francisco, E., & Luana, V. (2004). GIBBS: isothermal-isobaric
415 thermodynamics of solids from energy curves using a quasi-harmonic Debye
416 model. Computer Physics Communications, 158(1), 57-72.
- 417 Boness, D. A., Brown, J. M., & McMahan, A. K. (1986). The electronic
418 thermodynamics of iron under Earth core conditions. Physics of the Earth and
419 Planetary Interiors, 42(4), 227-240.
- 420 Caracas, R. (2015). The influence of hydrogen on the seismic properties of solid iron.
421 Geophysical Research Letters, 42(10), 3780-3785.
- 422 Dewaele, A., Loubeyre, P., Occelli, F., Mezouar, M., Dorogokupets, P. I., and Torrent,
423 M. (2006). Quasihydrostatic equation of state of iron above 2 Mbar. Physical
424 Review Letters, 97(21), 215504.
- 425 Dziewonski, A. M., and Anderson, D. L. (1981). Preliminary reference Earth model.
426 Physics of the earth and planetary interiors, 25(4), 297-356.

- 427 Fei, Y., Murphy, C., Shibazaki, Y., Shahar, A., and Huang, H. (2016). Thermal equation
428 of state of hcp-iron: Constraint on the density deficit of Earth's solid inner core.
429 Geophysical Research Letters, 43(13), 6837-6843.
- 430 Francisco, E., Recio, J. M., Blanco, M. A., Pendás, A. M., & Costales, A. (1998).
431 Quantum-mechanical study of thermodynamic and bonding properties of MgF₂.
432 The Journal of Physical Chemistry A, 102(9), 1595-1601.
- 433 Fukai, Y. (2006). The metal-hydrogen system: basic bulk properties. Springer.
- 434 Gomi, H., Fei, Y., and Yoshino, T. (2018). The effects of ferromagnetism and
435 interstitial hydrogen on the equation of states of hcp and dhcp FeH_x: Implications
436 for the Earth's inner core age. American Mineralogist: Journal of Earth and
437 Planetary Materials, 103(8), 1271-1281.
- 438 He, Y., Sun, S., Kim, D. Y., Jang, B. G., Li, H., & Mao, H. K. (2022). Superionic iron
439 alloys and their seismic velocities in Earth's inner core. Nature, 602(7896),
440 258-262.
- 441 Hirose, K., Wood, B., & Vočadlo, L. (2021). Light elements in the Earth's core. Nature
442 Reviews Earth & Environment, 2(9), 645-658.
- 443 Ikuta, D., Ohtani, E., Sano-Furukawa, A., Shibazaki, Y., Terasaki, H., Yuan, L., and
444 Hattori, T. (2019). Interstitial hydrogen atoms in face-centered cubic iron in the
445 Earth's core. Scientific Reports, 9(1), 7108, 1-8.
- 446 Isaev, E. I., Skorodumova, N. V., Ahuja, R., Vekilov, Y. K., and Johansson, B. (2007).
447 Dynamical stability of Fe-H in the Earth's mantle and core regions. Proceedings
448 of the National Academy of Sciences, 104(22), 9168-9171.

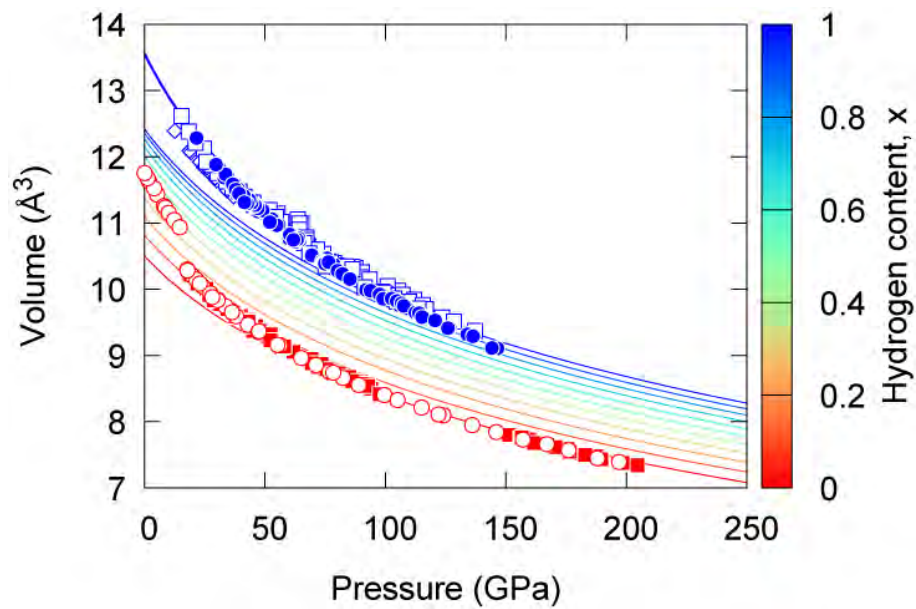
- 449 Kato, C., Umemoto, K., Ohta, K., Tagawa, S., Hirose, K., and Ohishi, Y. (2020).
450 Stability of fcc phase FeH to 137 GPa. *American Mineralogist: Journal of Earth*
451 *and Planetary Materials*, 105(6), 917-921.
- 452 Komabayashi, T., and Fei, Y. (2010). Internally consistent thermodynamic database for
453 iron to the Earth's core conditions. *Journal of Geophysical Research: Solid Earth*,
454 115(B3).
- 455 Leger, J. M., Loriers-Susse, C., and Vodar, B. (1972). Pressure effect on the Curie
456 temperatures of transition metals and alloys. *Physical Review B*, 6(11), 4250.
- 457 León, A., Velásquez, E. A., Torres, F. J., Mejía-López, J., and Vargas, P. (2020).
458 Hydrogen induced AFM to FM magnetic transition in ϵ -FeH_x. *Journal of*
459 *Magnetism and Magnetic Materials*, 498, 166147.
- 460 Li, Y., Vočadlo, L., Sun, T., and Brodholt, J. P. (2020). The Earth's core as a reservoir
461 of water. *Nature Geoscience*, 13(6), 453-458.
- 462 Machida, A., Saitoh, H., Sugimoto, H., Hattori, T., Sano-Furukawa, A., Endo, N.,
463 Katayama, Y., Iizuka, R., Sato, T., Matsuo, M., Orimo, S., & Aoki, K. (2014). Site
464 occupancy of interstitial deuterium atoms in face-centred cubic iron. *Nature*
465 *communications*, 5(1), 5063, 1-6.
- 466 Mao, W. L., Sturhahn, W., Heinz, D. L., Mao, H. K., Shu, J., and Hemley, R. J. (2004).
467 Nuclear resonant x - ray scattering of iron hydride at high pressure. *Geophysical*
468 *research letters*, 31(15).
- 469 Martorell, B., Brodholt, J., Wood, I. G., & Vočadlo, L. (2015). The elastic properties
470 and stability of fcc-Fe and fcc-FeNi alloys at inner-core conditions. *Geophysical*
471 *Journal International*, 202(1), 94-101.

- 472 Mitsui, T., and Hirao, N. (2010). Ultrahigh-pressure study on the magnetic state of iron
473 hydride using an energy domain synchrotron radiation ^{57}Fe Mössbauer
474 spectrometer. Materials Research Society Symposium Proceedings, 1262,
475 115-119.
- 476 Momma, K., and Izumi, F. (2011). VESTA 3 for three-dimensional visualization of
477 crystal, volumetric and morphology data. Journal of applied crystallography,
478 44(6), 1272-1276.
- 479 Mori, Y., Ozawa, H., Hirose, K., Sinmyo, R., Tateno, S., Morard, G., and Ohishi, Y.
480 (2017). Melting experiments on Fe–Fe₃S system to 254 GPa. Earth and Planetary
481 Science Letters, 464, 135-141.
- 482 Moruzzi, V. L., Janak, J. F., & Schwarz, K. (1988). Calculated thermal properties of
483 metals. Physical Review B, 37(2), 790.
- 484 Narygina, O., Dubrovinsky, L. S., McCammon, C. A., Kurnosov, A., Kantor, I. Y.,
485 Prakapenka, V. B., and Dubrovinskaia, N. A. (2011). X-ray diffraction and
486 Mössbauer spectroscopy study of fcc iron hydride FeH at high pressures and
487 implications for the composition of the Earth's core. Earth and Planetary Science
488 Letters, 307(3-4), 409-414.
- 489 Nasu, S., Sasaki, T., Kawakami, T., Tsutsui, T., and Endo, S. (2002). Mössbauer study
490 of ϵ -Fe under an external magnetic field. Journal of Physics: Condensed Matter,
491 14(44), 11167.
- 492 Onodera, A., Tsunoda, Y., Kunitomi, N., Pringle, O. A., Nicklow, R. M., and Moon, R.
493 M. (1994). Neutron-diffraction study of γ -Fe at high pressure. Physical Review B,
494 50(6), 3532.

- 495 Perdew, J. P., Burke, K., and Ernzerhof, M. (1996). Generalized gradient
496 approximation made simple. *Physical review letters*, 77(18), 3865.
- 497 Sakamaki, K., Takahashi, E., Nakajima, Y., Nishihara, Y., Funakoshi, K., Suzuki, T.,
498 and Fukai, Y. (2009). Melting phase relation of FeH_x up to 20 GPa: Implication
499 for the temperature of the Earth's core. *Physics of the Earth and Planetary*
500 *Interiors*, 174(1-4), 192-201.
- 501 Sato, K., Dederics, P. H., and Katayama-Yoshida, H. (2003). Curie temperatures of III–
502 V diluted magnetic semiconductors calculated from first principles. *EPL*
503 (*Europhysics Letters*), 61(3), 403.
- 504 Schneider, G., Baier, M., Wordel, R., Wagner, F. E., Antonov, V. E., Ponyatovsky, E. G.,
505 Kopilovskii, Yu. and Makarov, E. (1991). Mössbauer study of hydrides and
506 deuterides of iron and cobalt. *Journal of the Less Common Metals*, 172, 333-342.
- 507 Shibazaki, Y., Ohtani, E., Fukui, H., Sakai, T., Kamada, S., Ishikawa, D., Tsutsui, S.,
508 Baron, A.Q.R., Nishitani, N., Hirao, N., and Takemura, K. (2012). Sound velocity
509 measurements in dhcp-FeH up to 70 GPa with inelastic X-ray scattering:
510 Implications for the composition of the Earth's core. *Earth and Planetary Science*
511 *Letters*, 313, 79-85.
- 512 Shibazaki, Y., Ohtani, E., Terasaki, H., Tateyama, R., Sakamaki, T., Tsuchiya, T., and
513 Funakoshi, K. I. (2011). Effect of hydrogen on the melting temperature of FeS at
514 high pressure: Implications for the core of Ganymede. *Earth and Planetary*
515 *Science Letters*, 301(1-2), 153-158.
- 516 Shito, C., Kagi, H., Kakizawa, S., Aoki, K., Komatsu, K., Iizuka-Oku, R., Abe, J.,
517 Saitoh, H., Sano-Furukawa, A., & Hattori, T. (in press). Hydrogen occupation and

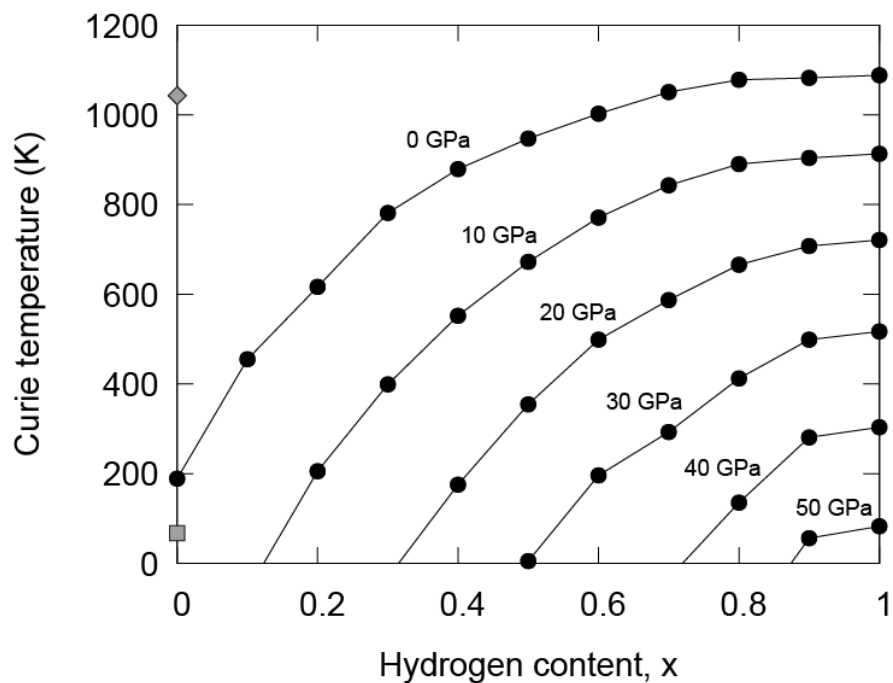
- 518 hydrogen-induced volume expansion in $\text{Fe}_{0.9}\text{Ni}_{0.1}\text{D}_x$ at high P - T conditions.
519 American Mineralogist.
- 520 Steinle-Neumann, G., Stixrude, L., and Cohen, R. E. (2004). Magnetism in dense
521 hexagonal iron. *Proceedings of the National Academy of Sciences*, 101(1), 33-36.
- 522 Sugimoto, H., and Fukai, Y. (1992). Solubility of hydrogen in metals under high
523 hydrogen pressures: thermodynamical calculations. *Acta metallurgica et*
524 *materialia*, 40(9), 2327-2336.
- 525 Tagawa, S., Gomi, H., Hirose, K., and Ohishi, Y. (2022). High-temperature equation of
526 state of FeH: Implications for hydrogen in Earth's inner core. *Geophysical*
527 *Research Letters*, 49(5), e2021GL096260.
- 528 Tagawa, S., Sakamoto, N., Hirose, K., Yokoo, S., Hernlund, J., Ohishi, Y., and
529 Yurimoto, H. (2021). Experimental evidence for hydrogen incorporation into
530 Earth's core. *Nature communications*, 12(1), 2588, 1-8.
- 531 Tateno, S., Hirose, K., Ohishi, Y., and Tatsumi, Y. (2010). The structure of iron in
532 Earth's inner core. *Science*, 330(6002), 359-361.
- 533 Thompson, E. C., Davis, A. H., Bi, W., Zhao, J., Alp, E. E., Zhang, D., Greenberg, E.,
534 Prakapenka, V. B., and Campbell, A. J. (2018). High - pressure geophysical
535 properties of Fcc phase FeH_x. *Geochemistry, Geophysics, Geosystems*, 19(1),
536 305-314.
- 537 Tsetseris, L. (2005). Noncollinear magnetism of iron along the tetragonal Bain
538 transformation. *Physical Review B*, 72(1), 012411.
- 539 Tsujino, N., Nishihara, Y., Nakajima, Y., Takahashi, E., Funakoshi, K. I., and Higo, Y.
540 (2013). Equation of state of γ -Fe: Reference density for planetary cores. *Earth and*
541 *Planetary Science Letters*, 375, 244-253.

- 542 Tsunoda, Y. (1989). Spin-density wave in cubic γ -Fe and γ -Fe_{100-x}Co_x precipitates in Cu.
543 Journal of Physics: Condensed Matter, 1(51), 10427.
- 544 Wakamatsu, T., Ohta, K., Tagawa, S., Yagi, T., Hirose, K., & Ohishi, Y. (2022).
545 Compressional wave velocity for iron hydrides to 100 gigapascals via picosecond
546 acoustics. Physics and Chemistry of Minerals, 49(5), 1-11.
- 547 Yuan, L., and Steinle-Neumann, G. (2020). Strong sequestration of hydrogen into the
548 Earth's core during planetary differentiation. Geophysical Research Letters,
549 47(15), e2020GL088303.
550



551

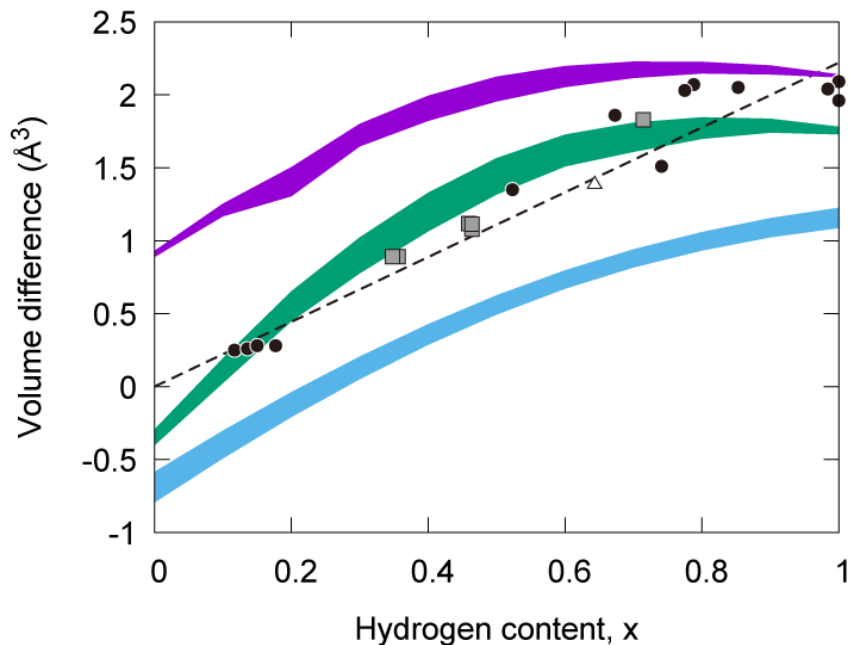
552 **Figure 1.** Equation of states of fcc FeH_x . Thick blue line is FM FeH . Thin solid lines
553 are NM FeH_x ($x = 0.0, 0.1, \dots, 1.0$). Colors represent the composition from pure Fe
554 (red) to FeH (blue). Previous experimental data are also plotted for comparison. Blue
555 diamonds: fcc FeH (Narygina et al. 2011). Blue circles: fcc FeH (Tagawa et al. 2022).
556 Blue squares: fcc FeH (Kato et al. 2020). Red circles: bcc and hcp Fe (Dewaele et al.
557 2006). Red squares: hcp Fe (Fei et al. 2016).
558



559

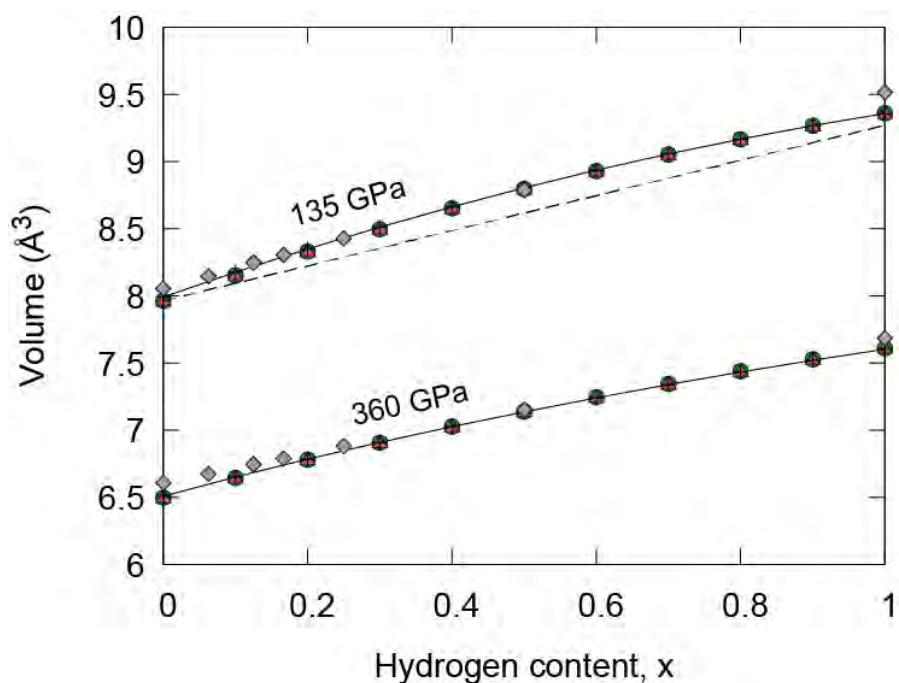
560 **Figure 2.** Curie temperature of FM fcc FeH_x as functions of pressure and hydrogen
561 content (black circles). Curie temperature of bcc Fe (gray diamond) (Leger et al. 1972)
562 and Néel temperature of SDW fcc Fe (gray square) (Onodera et al. 1994) are also
563 plotted for comparison.

564



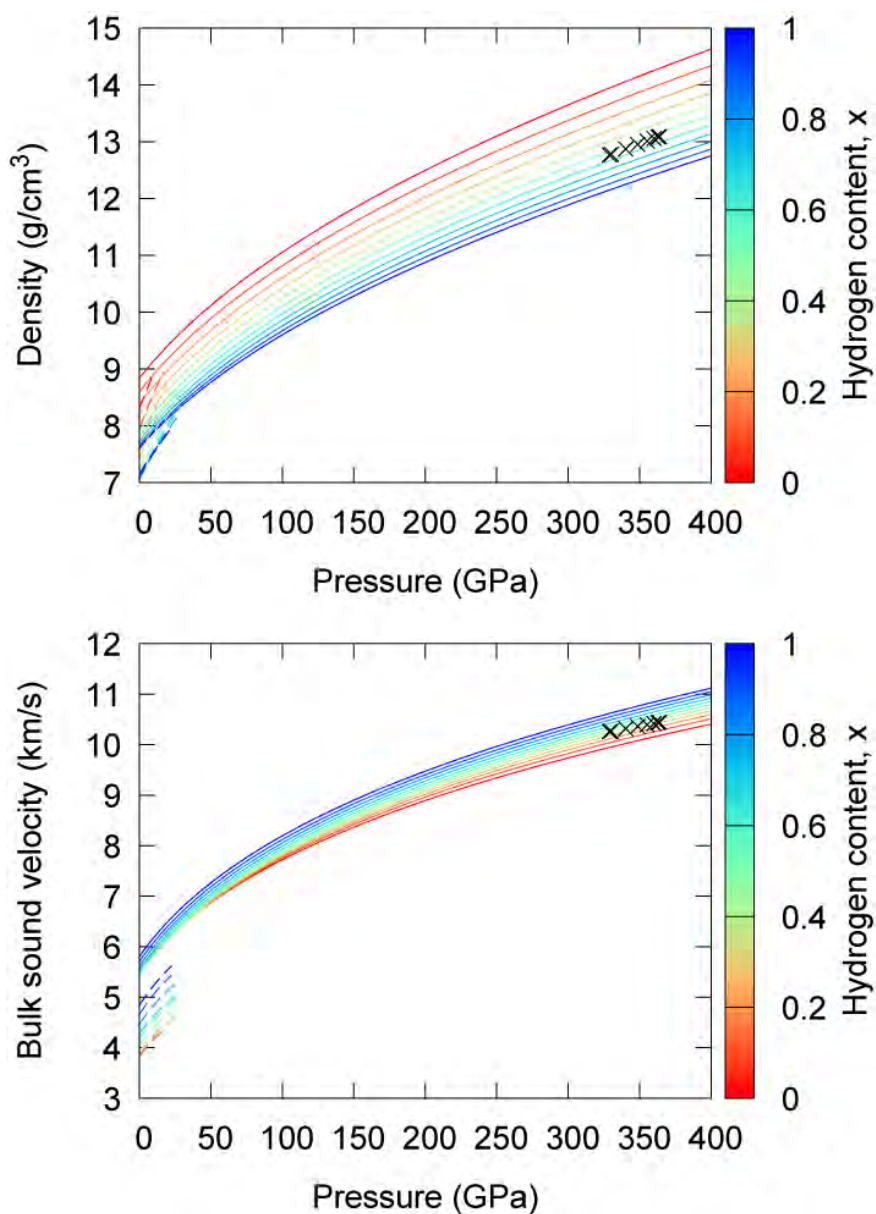
565

566 **Figure 3.** Volume difference between FeH_x (Ikuta et al. 2019, Machida et al. 2014, and
567 present calculations) and fcc Fe (Tsujino et al. 2016). Each reference volume of fcc Fe
568 (Tsujino et al. 2016) is calculated at the pressure and temperature conditions identical
569 to that of the FeH_x data point. Purple (FM), green (LMD), and cyan (NM) bands are
570 present calculations at the pressure range of 3.8-12.3 GPa. Black circles are previous
571 experiments for fcc FeH_x at $P = 3.8\text{-}12.3$ GPa and $T = 750\text{-}1200$ K (Ikuta et al. 2019).
572 An open triangle indicates hcp FeH_x at $P = 6.3$ GPa and $T = 988$ K (Machida et al.
573 2014). Gray squares represent the volume difference between fcc $\text{Fe}_{0.9}\text{Ni}_{0.1}\text{H}_x$ and fcc
574 $\text{Fe}_{0.9}\text{Ni}_{0.1}$ at $P = 6.3\text{-}11.7$ GPa and $T = 500\text{-}950$ K (Shito et al. in press). The broken
575 line indicates the linear expansion model with $\Delta V_{\text{H}} = 2.22 \text{ \AA}^3$ (Ikuta et al. 2019).
576



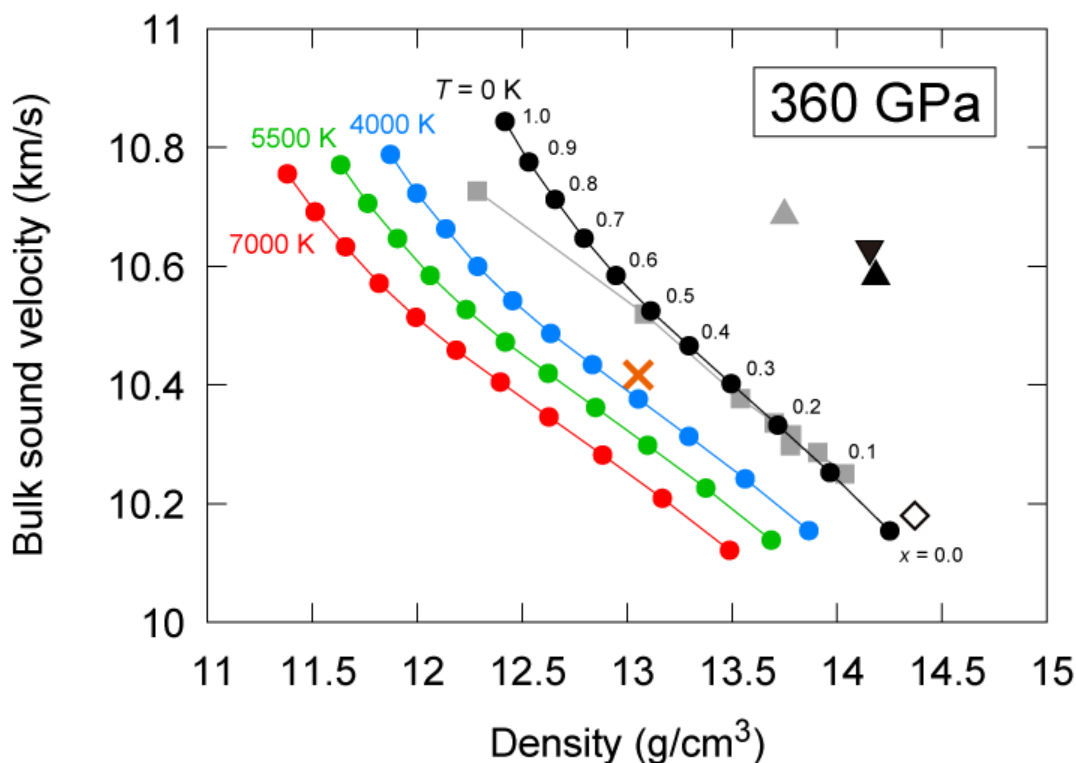
577

578 **Figure 4.** Volume of NM FeH_x at 135 and 360 GPa with fcc (cross symbol with solid
579 line), hcp (orange triangle) and dhcp (green circle) crystal structures. Note that
580 volumes of these three structures are almost identical. Gray diamond symbols indicate
581 the previous supercell calculation on hcp FeH_x (Caracas 2015). The broken line is a
582 linear interpolation of previous diamond-anvil cell experiments between hcp Fe
583 (Dewaele et al. 2006) and fcc FeH (Tagawa et al. 2022) at 135 GPa.
584



585

586 **Figure 5.** (a) Density and (b) bulk sound velocity of NM (solid lines) and LMD
587 (broken lines) fcc FeH_x ($x = 0.0, 0.1, 0.2, \dots, 1.0$) as functions of pressure. Colors
588 represent the composition from pure Fe (red) to FeH (blue). Cross symbols indicated
589 the PREM at the inner core (Dziewonski and Anderson 1981).
590



591

592 **Figure 6.** The density-bulk sound velocity relationship at 360 GPa. Black circles are
593 present calculations for fcc FeH_x at 0 K. Note that the hydrogen content (x) increases
594 from the bottom right to the top left. Previous low-temperature data are also plotted for
595 comparison. Gray squares are hcp FeH_x at 0 K from Caracas (2015). Open diamond is
596 calculated from the experimental equation of states for hcp Fe at 300 K (Dewaele et al.
597 2006). Black triangle and inverted triangle are hcp and fcc Fe at 0 K, respectively
598 (Martorell et al. 2015). Gray triangle is hcp $\text{FeH}_{0.25}$ at 0K (He et al. 2022). Blue, green,
599 and red circles are present calculation at 4000, 5500, and 7000 K, respectively,
600 assuming that the Poisson's ratio is equal to the PREM value (see main text for detail).
601 The orange cross symbol indicates the PREM at the inner core (Dziewonski and
602 Anderson 1981).